

Lifshitz Transition and Band Structure Evolution in Alkali Metal Intercalated 1T'-MoTe₂

Joohyung Park,¹ Ayan N. Batyrkhanov,¹ Jonas Brandhoff,³ Marco Gruenewald,³ Felix Otto,³ Maximilian Schaal,³ Saban Hus,⁴ Torsten Fritz,^{1,3} Florian Göttl,² An-Ping Li⁴, and Oliver L.A. Monti^{1,5,*}

Affiliations

¹ Department of Chemistry and Biochemistry, University of Arizona, Tucson, Arizona, 85721, USA

² Department of Biosystems Engineering, University of Arizona, Tucson, Arizona, 85721, USA

³ Institute of Solid State Physics, Friedrich Schiller University Jena, 07743 Jena, Germany

⁴ Center for Nanophase Materials Sciences, Oak Ridge National Laboratory, Oak Ridge, Tennessee 37831, USA

⁵ Department of Physics, University of Arizona, Tucson, Arizona, 85721, USA

Abstract

In van der Waals materials, coupling between adjacent layers is weak, and consequently interlayer interactions are weakly screened. This opens the possibility to profoundly modify the electronic structure e.g. by applying electric fields or with adsorbates. Here, we show for the case of the topologically trivial semimetal 1T'-MoTe₂ that potassium dosing significantly transforms its band structure. With a combination of angle-resolved photoemission spectroscopy, scanning tunneling microscopy, x-ray spectroscopy and density functional theory we show that MoTe₂ undergoes a Lifshitz transition where the electronic structure shifts rigidly for small concentrations of K, while for larger concentrations MoTe₂ undergoes significant band structure evolution. Our results demonstrate that the origin of this electronic structure change stems from alkali metal intercalation which effectively decouples the 2D sheets and brings K-intercalated 1T'-MoTe₂ to the quasi-2D limit.

Introduction

Modifying and controlling the properties of quantum materials by external stimuli or by interfacing them with other materials offers enormous opportunities to create materials by design for novel functionalities with electronic and spintronic applications. This is particularly true for van der Waals layered materials where such control is available to an unsurpassed extent, with the aim of tailoring electronic correlations. To achieve this goal, many different approaches have been employed: For atomically thin materials, strain may be used to control, e.g., the bandgap [1,2]; doping may lead to significant electronic structure changes [3,4]; formation of layered heterostructures with other 2D materials can reveal novel exotic electronic phases [5-7]; proximitization with organic molecules may manipulate spin and other degrees of freedom [8,9]; and ultrafast laser excitation may access hidden phases [10,11]. A particularly simple and effective approach is the modification by adsorption of alkali metal atoms, whose low ionization energy enables strong electron doping, and whose small size may allow for intercalation and strong hybridization within the van der Waals gap [12-16]. The consequences of decorating van der Waals materials vary enormously, depending significantly on the specifics of the pristine phase, and range from simple doping to drastic changes in band structure.

Though this has been recognized for some time for van der Waals layered semiconductors, the influence of alkali adsorbates and intercalation on layered semimetals is less clear due to the lack of a fundamental gap and the increased screening due to a higher carrier density. In addition, the near-balanced coexistence of electron and hole pockets in semimetals adds a further dimension. In van der Waals materials, the layer separation constitutes an important degree of freedom with potentially direct consequences for the electronic structure. Indeed, recent evidence suggests that alkali metals can act as electron dopants and chemical gates in van der Waals layered semimetals [12,13]. This is important

because the charge carrier density in semimetals can control associated many-body phenomena such as superconductivity, charge-density waves, and quantum hall states [17-19]. Further, changing the electron density may also cause a Lifshitz transition, an electronic topological transition at the Fermi surface. Such a transition leads to abrupt changes in thermodynamic, elastic, and transport properties [20].

In a recent study, dosing of an alkali metal on semimetal T_d -WTe₂ has shown that this not only increases electron concentration but also induces shear displacement in the crystal structure to change the crystal symmetry [21]. $1T'$ -MoTe₂ is ideally poised for such a structural transition as well, since this occurs naturally at ~ 250 K [22,23]. Importantly, the resulting T_d phase constitutes a Weyl semimetal. Moreover, its charge carrier density changes as a function of temperature, achieving a nearly compensated semimetal phase below 50 K due to the expansion of the hole pocket [24-26]. Recent work shows that atomic dosing e.g. of iron p-dopes MoTe₂, changing the ratio of electron and hole pocket sizes dramatically and over a wide temperature range [27]. Alkali atom dosing may thus reveal important ways for controlling and tailoring the electronic structure of MoTe₂.

Here, we use angle-resolved photoemission spectroscopy (ARPES) to study the changes in the band structure in $1T'$ -MoTe₂ as a function of dosing with potassium atoms. We show that potassiation gives rise to a Lifshitz transition, which also involves a rigid band shift and, at higher dosing, a significant transformation of the band structure. By combining density functional theory (DFT), angle-dependent x-ray photoemission spectroscopy (AD-XPS), and scanning tunneling microscopy (STM), we argue that these changes are caused primarily by intercalation and the ensuing layer decoupling, demonstrating the potential of alkali atoms to tailor electronic properties of layered semimetals.

The manuscript is structured as follows: First, we present ARPES data showing how the electronic structure of $1T'$ -MoTe₂ changes upon potassiation. Next, we computationally study the thermodynamics and structural changes of $1T'$ -MoTe₂ as a result of potassiation and use these insights

together with ARPES and other surface-sensitive techniques to demonstrate layer decoupling caused by intercalation. This allows us to draw a comprehensive picture of the impact of potassiation on 1T'-MoTe₂ and discuss the implications of our results.

Methods

Sample Preparation

The 1T'-MoTe₂ crystal was sourced from HQ Graphene and mounted to an Omicron style sample flag using conductive double-sided copper tape. The crystal was freshly exfoliated under high vacuum (mid 10⁻⁹ mbar) using the Scotch tape method, and then introduced to ultrahigh vacuum (low 10⁻¹⁰ mbar). Potassium was deposited at ambient temperature from an SAES getter source in a separate preparation chamber with a typical base pressure of 1x10⁻¹⁰ mbar. Stepwise deposition cycles were taken to increase the amount of potassium, followed immediately by acquisition of the ARPES maps to minimize the impact of potassium diffusion into the bulk crystal. In this way, spectra remained stable over the course of successive sequential potassiation steps.

LEED Image Acquisitions and Analysis

Low-electron energy diffraction images were acquired using a SPECTRALEED (Omicron) with electron energy of 80 eV at room temperature. Post acquisition image correction such as distortion correction was done by the freely available software LEEDCal, whereas the quantitative determination of the unit cell parameters was performed using LEEDLab [28].

DFT Computations

All calculations were carried out using the Vienna Ab-Initio Simulation package (VASP) [29,30], a plane wave code using PAW pseudopotentials [31,32]), with the PBE functional [33] and TS dispersion

corrections [34]. In our calculations we used a k -point grid of $15 \times 9 \times 3$ for a single unit cell. In slab calculations, k -points in the z -direction were reduced to 1. In structural optimizations, the x and y lattice vectors in a 1×2 unit cell were optimized manually first, then the z -direction was optimized manually. As a final optimization step, the unit cell was allowed to relax. Band structures were separately calculated for 40 k -points along the ΓX , ΓY , and ΓS direction.

Ultraviolet Photoemission Spectroscopy and Angle-Resolved Photoemission

Spectroscopy

The crystal was aligned along the high symmetry directions ($\overline{\Gamma X}$, $\overline{Y\Gamma}$, and $\overline{\Gamma S}$) using LEED. Ultraviolet photoemission spectroscopy (UPS) and angle-resolved photoemission spectroscopy data was collected with a non-monochromatized He discharge lamp (SPECS 10/35) mounted at 30° angle of incidence in a VG ESCALab MK II photoemission spectrometer, with an instrumental resolution of 120 meV. All spectra were acquired at room temperature by successively tilting the sample along the polar angle. A sample bias of -5 V was applied during the data acquisition. The acceptance angle was $\pm 1.5^\circ$ ($\Delta k_{\parallel} \approx \pm 0.055 \text{ \AA}^{-1}$ at Fermi level).

Angle-Dependent X-ray Photoemission Spectroscopy

Surface analysis was conducted using a SPECS Surface Nano Analysis GmbH system with a PHOIBOS 150 hemispherical analyzer and a three-dimensional delay-line detector. A Focus 500 (SEPCS GmbH, monochromatized Al K α emission: 1486.71 eV) was used as an x-ray source with a relative angle to the analyzer of 55° . The acceptance angle of the analyzer was $\pm 8^\circ$. The maximum amount of potassium dosing was determined by a quartz crystal microbalance (Tetra GmbH), calibrated to the appearance of the (2×2) superstructure of K-intercalated 1 ML epitaxial graphene on SiC(0001) [35].

Scanning Tunneling Microscopy

STM measurements were performed with a variable-temperature STM system (Scienta Omicron VT-STM) operated at room temperature. Electrochemically etched tungsten tips were used as STM probes. The quality and sharpness of the STM tips were tested with STM/STS measurements on a clean Cu(100) surface before being used on the MoTe₂ surface.

Results

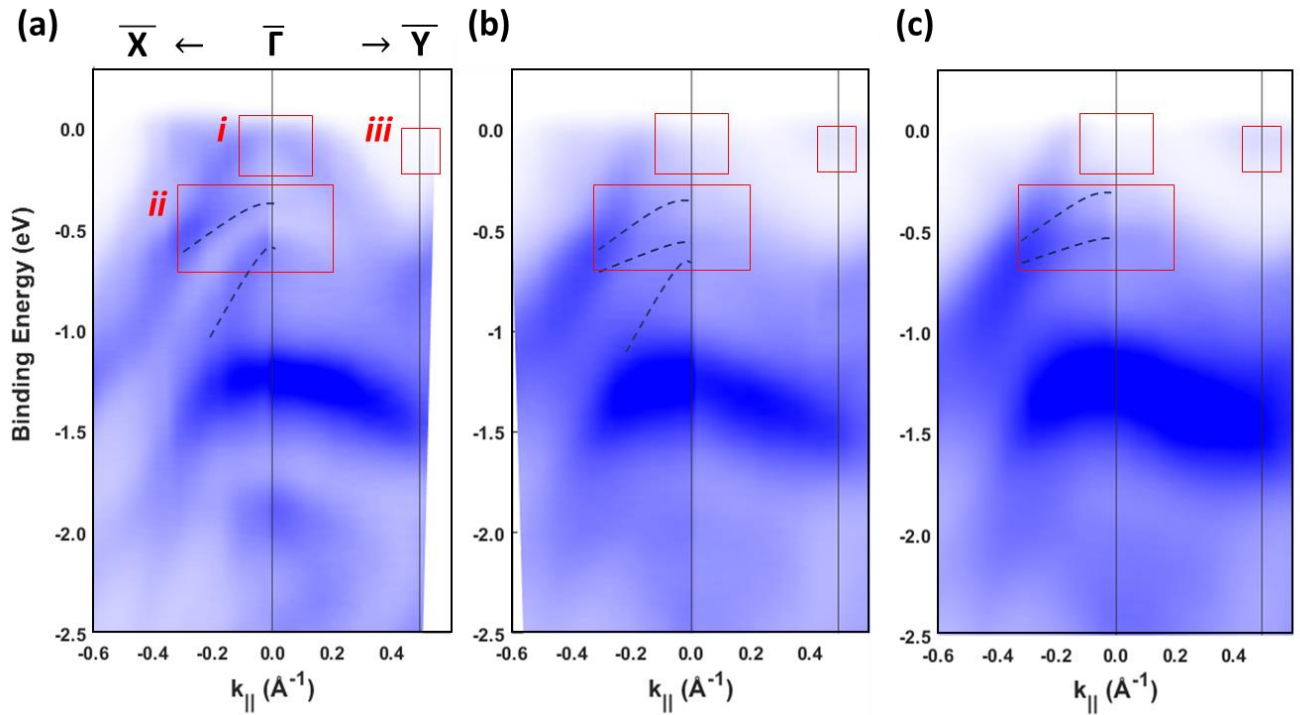


Fig. 1. ARPES maps of select representative potassiated samples. $\overline{\Gamma\bar{X}}$ and $\overline{\Gamma\bar{Y}}$ maps of (a) Pristine, (b) K75, and (c) K255. See main text for definition of sample labeling. Three regions of interest are indicated in red boxes and dashed lines are a guide to the eye for region (ii) in all three panels.

We first focus on spectroscopic results of the effect of potassium dosing on 1T'-MoTe₂. Fig 1 shows ARPES maps of a few samples that represent the key changes in the band structure. Since K atoms may adsorb at the surface or intercalate, we prefer to label each sample in terms of the K

deposition time in seconds rather than in some likely fictitious fractional monolayer coverage: K75 indicates 75 seconds and K255 indicates 255 seconds of cumulative potassiation of the sample. Fig 1 (a) shows the band structure of pristine 1T'-MoTe₂ along the two high symmetry directions $\bar{\Gamma}\bar{X}$ and $\bar{\Gamma}\bar{Y}$. It matches well with previous ARPES data, and the diffraction pattern from LEED shows the expected high degree of crystalline order (Supplemental Material Fig S1) [23,36]. In Fig 1 (a), we label three regions of interest with red boxes and roman numerals, where pronounced changes appear as a consequence of potassium deposition. Comparing the ARPES map of the K255 structure to the pristine sample (see Fig 1 (a) and 1 (c)), we find that in region (i), bands near the Fermi level at the $\bar{\Gamma}$ point disappear almost completely upon K deposition. Further, in region (ii), the band dispersions change, flattening the lower band and sharpening the upper bands, opposite to the pristine structure. Lastly, in region (iii), a new band appears near the Fermi level at the \bar{Y} point, indicating the occurrence of a Lifshitz transition, caused by the change of the topology of Fermi surface. The K75 ARPES map (Fig 1 (b)) bridges the two bookends of pristine and K255 MoTe₂: It already hosts the new band at \bar{Y} , and bands near the Fermi level at $\bar{\Gamma}$ are fainter than in the pristine sample, though the structure at $\bar{\Gamma}$ near a binding energy of -0.5eV is too diffuse to compare to either pristine or K255 MoTe₂. Thus, K75 represents an intermediate state between pristine and K255 MoTe₂.

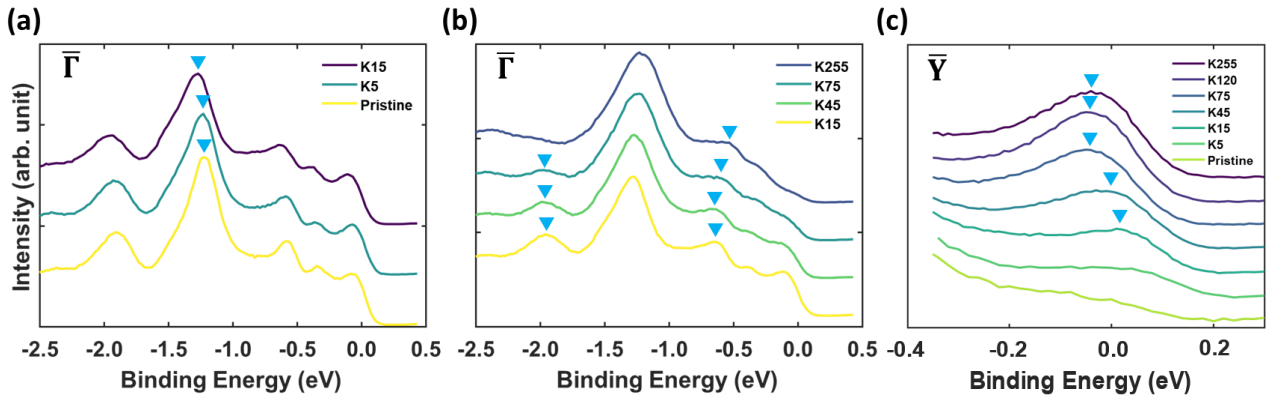


FIG. 2. UPS stacks of potassiated samples measured at high symmetry points. (a) Small dosing limit: Pristine, K5, and K15 at $\bar{\Gamma}$. (b) Higher dosing limit: K15, K45, K75, and K255 at $\bar{\Gamma}$. K15 is included to

illustrate the band structure evolution. (c) Changes in the electron pocket at \bar{Y} . A triangle shape is used as guide to the eye for the peak position shifts in the spectra. Note that colors do not correspond to the same dosing across different panels.

To gain deeper understanding of the electronic structure change, we directly compare spectra with different amounts of potassium for two different points in the Brillouin zone. Fig 2 (a) and (b) show the band structure evolution at $\bar{\Gamma}$ in the first 2.5 eV below E_F , for the case of low potassium dosing and across a wider range of potassium dosing, respectively. Initially for lower potassium dosing, the bands shift monotonically to higher binding energies for all the observed features in the spectra, by 9 ± 4 meV for K5 and 44 ± 7 meV for K15, as obtained from Gaussian peak fit of the main features after Shirley background subtraction. From the fact that the peak shifts are monotonic and that the spectra show only moderate broadening, the low concentration potassium limit can be understood as doping, though as mentioned below accompanied by a Lifshitz transition. More drastic changes occur at higher doses of K on MoTe₂: *i)* The peak positions shift non-uniformly, e.g., the band at a binding energy of -1.9 eV shifts further below E_F , whereas the band at a binding energy of -0.6 eV shifts closer to E_F . *ii)* Peaks broaden with increasing K coverage. *iii)* The photoemission intensity of the bands near the Fermi level diminishes at the $\bar{\Gamma}$ point. Consequently, after the Lifshitz transition that occurs already at the lowest dosing levels, further evolution of the band structure continues to be significant and occurs throughout the Brillouin zone, including a continued growth of the electron pocket at \bar{Y} (Fig 2(c)). Such changes to the band structure, from rigid band shifts to overall changes, is a likely a consequence of the weak interlayer interaction in MoTe₂ and a remarkable feature of other layered semimetals as well, although there the details may vary depending on the materials and preparations [12,13,21].

Considering the electron pocket at \bar{Y} in more detail, we note that it shifts farther below E_F at higher potassium, until saturating at the higher dosing (K75 and higher). We note that the electron pocket develops a pronounced long tail towards higher binding energies (see Fig S2) for higher degrees

of potassiation. This likely involves changes to the electron-phonon interaction strength, since theoretical studies find that an increased number of electrons in a MoTe_2 sheet results in stronger electron-phonon interactions [37-39]. In summary, the band structure evolution depends on the specific location in the Brillouin zone: Some bands keep showing signatures of significant band structure change up to K255 (e.g. at $\bar{\Gamma}$), other bands saturate earlier at K75 (e.g. the electron pocket at \bar{Y}). Our ARPES and UPS data show that the MoTe_2 band structure evolves with potassiation in a complex way.

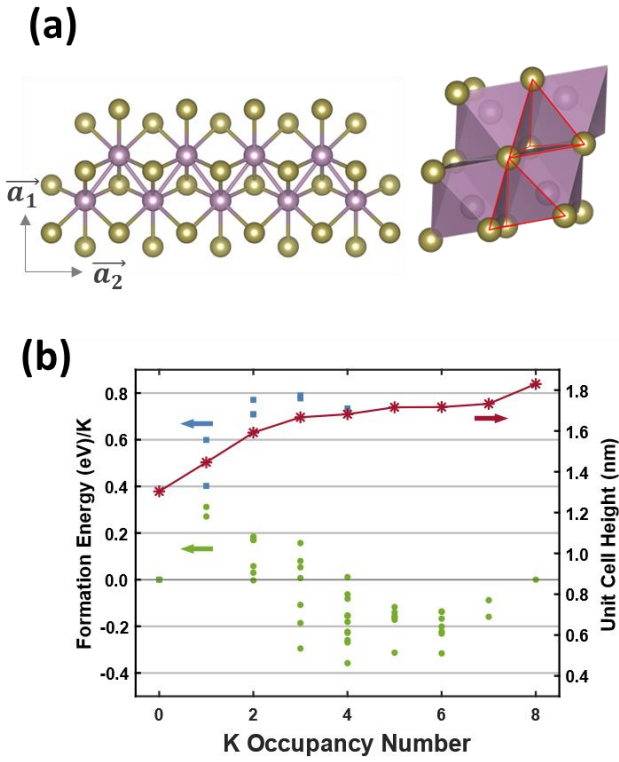


FIG. 3. Structural considerations and DFT analysis. (a) Left: Top-down view of the crystal structure of $1T'$ - MoTe_2 . Mo: purple, Te: gold. Right: Cartoon of the crystal structure. (b) DFT calculation of the thermodynamics of potassiation ($U = 0$ eV). Light green: Formation energy of potassium intercalation as a function of K occupancy number in a 1×2 superstructure. Light blue: The same for a surface adsorbate. The scattered dots indicate the formation energy from different configurations in the supercell. Dark red line: Unit cell height per K occupancy number in the optimized bulk structure.

To investigate the changes to the electronic structure of MoTe_2 upon K deposition, we use DFT+U calculations. First, we focus on pristine $1T'$ - MoTe_2 . Each bulk unit cell consists of two MoTe_2 sheets, and the unit cell of a single MoTe_2 sheet contains two inequivalent Mo atoms that establish a zig-

zag network in the \vec{a}_2 direction (Fig. 3 (a)). Each Mo atom is coordinated by six Te atoms forming a distorted octahedron of which three Te atoms create the triangular face of the surface 2D sheet (bright faces in cartoon, Fig. 3 (a)). Adjacent to each octahedron is a tetragonal void, of which there are two in each unit cell (highlighted with red lines). The relative spacing of the layers is determined by the c-axis of the unit cell, normal to the MoTe₂ layers.

In order to find an optimal computational setup, we vary two parameters: The Hubbard U and the c-axis of the unit cell. U corrects for a shortcoming in semi-local GGA approximations to correctly describe the d-states of Mo, while the c-axis of the unit cell depends on the correct description of long-range dispersion forces, which are by definition not captured correctly by semi-local approximations. By comparing the ARPES maps with the DFT calculations, we find the best agreement between experiment and DFT with a U of 2.0 eV, and a c-axis unit cell spacing of 14.2 Å. Details considering this parameterization and the comparison with experiment are given in Fig. S3 and S4.

We first seek to understand the nature of the thermodynamically most favored structure of K-MoTe₂. Here, we consider two situations as relevant limiting cases, namely 1) surface adsorption and 2) bulk intercalation. In order to study different K loadings and search a large structural space, we initially focus on a 1×2 supercell to allow nearest neighboring lattice interactions along the molybdenum zig-zag network. Also, from our structural considerations, we assume a maximum K loading of 1 K/Mo. For surface adsorption, this leads to a maximum of four K atoms per supercell, and for bulk intercalation to a maximum of eight K atoms per supercell. We then investigate all possible permutations for one to four (or eight) K atoms per supercell and show the formation energy/K atom as well as the c-axis value of the intercalated bulk unit cell in Fig. 3(b). We define formation energy per potassium as

$$E_{form/K} = (E_{MoTe_2+nK} - E_{MoTe_2} - n \times \mu_K^{MoTe_2+8K})/n \quad (1)$$

with

$$\mu_K^{MoTe_2+8K} = (E_{MoTe_2+8K} - E_{MoTe_2})/8 \quad (2)$$

for the example of potassium intercalated bulk MoTe₂. Here n is the occupancy number, E_{MoTe_2+nK} indicates the total energy of MoTe₂ lattice with a certain potassium occupancy number n , and $\mu_K^{MoTe_2+8K}$ is the chemical potential of potassiated MoTe₂ with an occupancy number of eight, as defined in eq. 2. In the case of the surface adsorbate, $n_{max} = 4$ instead of 8. This sets the formation energy of K to zero for occupancy numbers 0 and 8, thereby defining maximum potassiation as the relevant thermodynamic reference state [40]. $E_{form/K}$ expresses therefore the energy gain of partially potassiated structures (surface adsorption or intercalation) relative to the fully potassiated bulk MoTe₂ crystal that may only be realized with essentially infinite amounts of K. Note also that these calculations are carried out for $U = 0$ eV, since the value of U has no impact on the overall behavior of the formation energy.

The results of this analysis illustrate two important points: First, surface adsorption of K on MoTe₂ is *always* less favorable than intercalation. Second, an occupancy number around four in the intercalation scenario is thermodynamically the most favorable configuration, though three or higher cannot be excluded as they all offer thermodynamic gain. In contrast, introducing only one or two K atoms in the system involves either an energy penalty or no gain in stability. This implies that at low K loadings, K atoms may not spread uniformly into the lattice but rather form local intercalated clusters of higher potassium density. This local clusters picture might qualitatively explain small peak broadenings found in both K5 and K15 samples in Fig. 2 (a). Similar findings on thermodynamically lower stabilities at smaller alkali metal loadings have also been reported for other systems, though the formation energy trends are not universal due to sometimes different reference states considered for calculating the formation energy [14,40].

The calculated crystal structure from the most stable configuration also provides evidence that

three to six is the preferred occupancy number: When considering the c-axis dimension upon intercalation (see Fig. 3 (b)), we find a consistent increase in unit cell height at smaller occupancy numbers. However, as the occupancy number reaches four, the c-axis dimension levels off, before increasing again at seven and eight. Structurally, this indicates an effective increase of the layer separation of adjacent MoTe₂ layers that saturates around four K, and implies that K intercalation results in an effective layer decoupling, with severe consequences for the electronic structure.

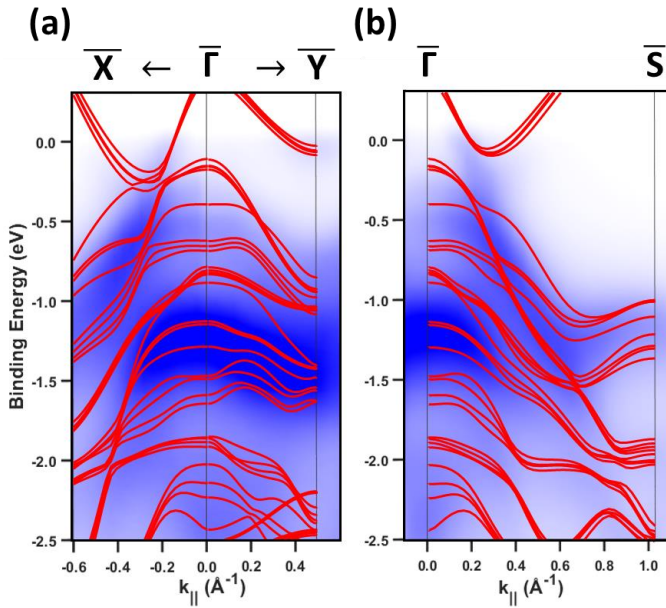


FIG. 4. Overlay between the optimized electronic band structure (occupancy number of four, red lines) and the K255 ARPES maps. (a) High symmetry directions $\overline{\Gamma\bar{X}}$ and $\overline{\Gamma\bar{Y}}$. Note that \bar{X} is not reached. (b) High symmetry direction $\overline{\Gamma\bar{S}}$.

With these structural and thermodynamic considerations in mind, we calculate the band structure for the half-filled (occupation number 4), fully filled (occupation number 8) and surface-potassiated MoTe₂ for comparison with our experimental data. For this purpose, we focus on a four-layer slab with a 1×1 unit cell (see Fig. S5 for the DFT optimized crystal structures and band structures using slab calculation). Slab calculations are appropriate since they reflect the surface-sensitive nature of photoemission spectroscopy. Also, the 1×1 unit cell captures the nature of the most stable K configurations and describes the experimentally observed Brillouin zone size as we don't observe

signatures of superlattice formation and zone folding. When finding the best matching occupancy number compared to the ARPES map of K255 sample, we revisit the Hubbard U , since there is a possibility that the presence of potassium changes the chemical nature of the Mo atoms. However, we find that a Hubbard U value of 2.0 eV is still valid. We then compare the DFT band structures to the ARPES maps of the K255 sample. In agreement with the thermodynamic data, we find that band structures for occupancy number of four (half-filling, 0.5 K / Mo atom) show good agreement with experiments in all the momentum space directions investigated (see Fig. 4 (a) and (b)). Additionally, we note that the possibility of full occupancy (occupation number eight) and surface-adsorbed K as an alternative explanation of the experimentally observed band structures can be safely excluded by comparing e.g. the bands found at high symmetry points such as \bar{Y} and \bar{S} , where unacceptable spurious bands appear in the DFT band maps (see Fig. S5 (b) – (d) for the relevant band structures).

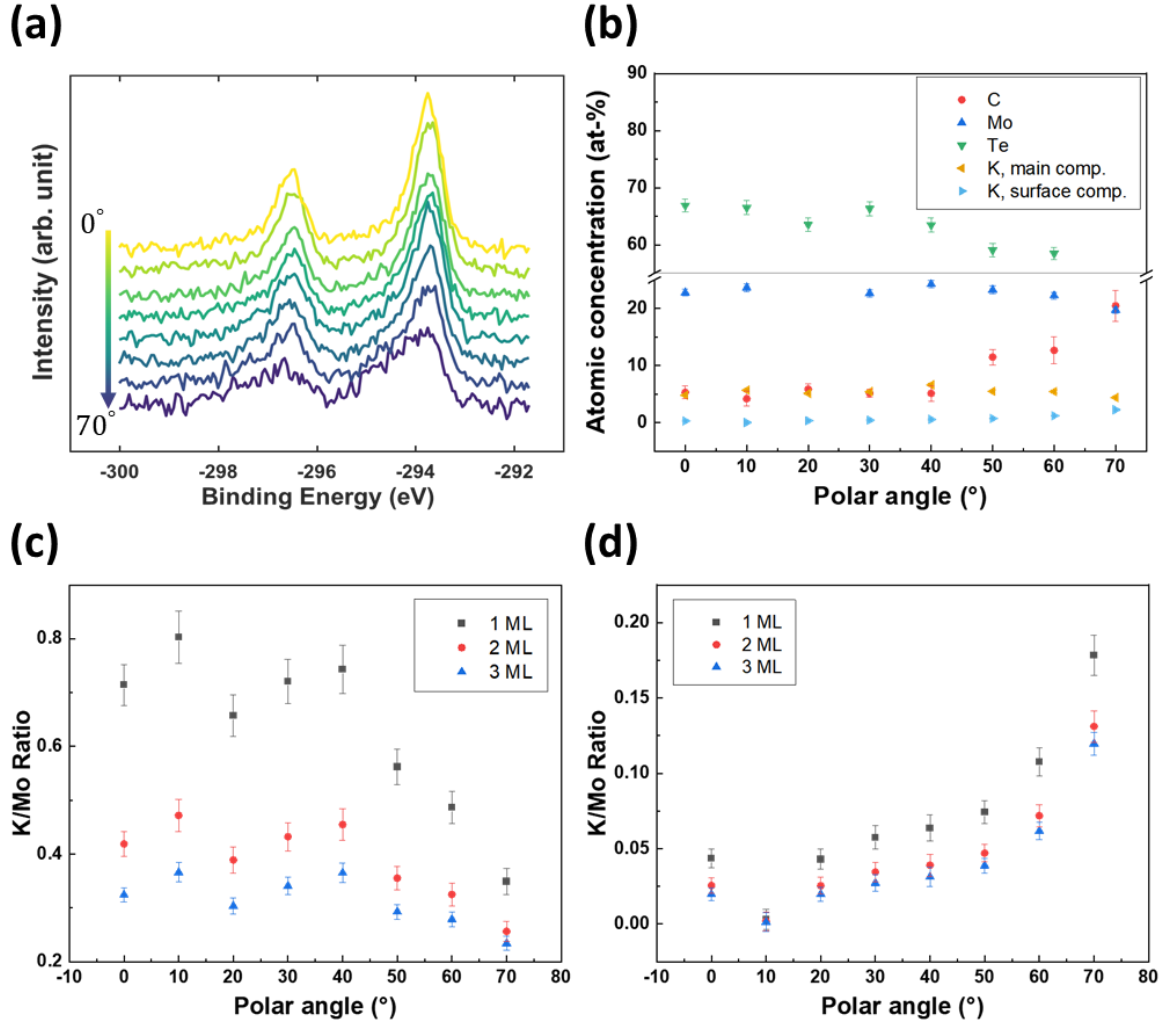


FIG. 5. AD-XPS of $K-MoTe_2$. (a) Angle-dependent $K 2p$ spectra of a highly potassiated sample. From top to bottom: Emission angle of 0 to 70 degrees, with 10 degrees step size. (b) Angular variation of the detected elemental atomic concentrations. (c) and (d) K to Mo ratios assuming an $MoTe_2$ thickness of 1 ML, 2 ML, and 3 ML, where the main component K is used in (c), and the surface component K is used in (d).

We use angle-dependent XPS (AD-XPS) to test our hypothesis of predominant K intercalation. By varying the photoemission take-off angle, the XPS data gives depth-related information from near the surface of $MoTe_2$. Fig. 5(a) shows angle-dependent background-subtracted AD-XPS of $K 2p$. From the $K 2p$ peaks obtained at different take-off angles, we observe that the $2p_{3/2}$ and $2p_{1/2}$ profile develops an additional component at higher emission angles, in coexistence with the main component. This is

suggestive of the existence of two different chemical environments of the K atoms. We propose that the two components correspond to a minor contribution of surface adsorbate in the presence of an intercalated species (main component). Using relative sensitivity factors [41], Fig. 5(b) shows atomic concentrations determined for each of these two components as well as for other detected elements as a function of take-off angle. Recognizing that there is a small contribution of surface-confined carbon contamination, neither Te nor Mo features show a pronounced angle dependence, consistent with the homogeneous bulk nature of MoTe_2 . For potassium, the main component is present at all angles. In contrast, the minor component remains almost non-existent at lower angles and increases only at higher angles. This indicates that the minor component is indeed likely to correspond to a small contribution of surface adsorbed potassium. By taking the inelastic mean free path and information depth of XPS into account [42,43], we see that the majority of the main potassium component resides away from the surface. The corresponding K atoms are most likely found between the surface layer and either the 2nd or 3rd layer of MoTe_2 , in contrast to the surface potassium component (Fig. 5(c) and (d)). To test if the ratio of surface-bound and intercalated K changes with degree of potassiation, we doubled the amount of deposited potassium. The relative atomic concentrations do not differ (Fig. S6), suggesting that once potassiation of MoTe_2 reaches a point where maximum thermodynamic gain occurs, e.g. an occupancy number of four as suggested by DFT, additional potassium atoms diffuse to deeper layers. AD-XPS therefore supports the notion of a majority intercalation of potassium below the surface, in the presence of a minor component of a surface adsorbate.

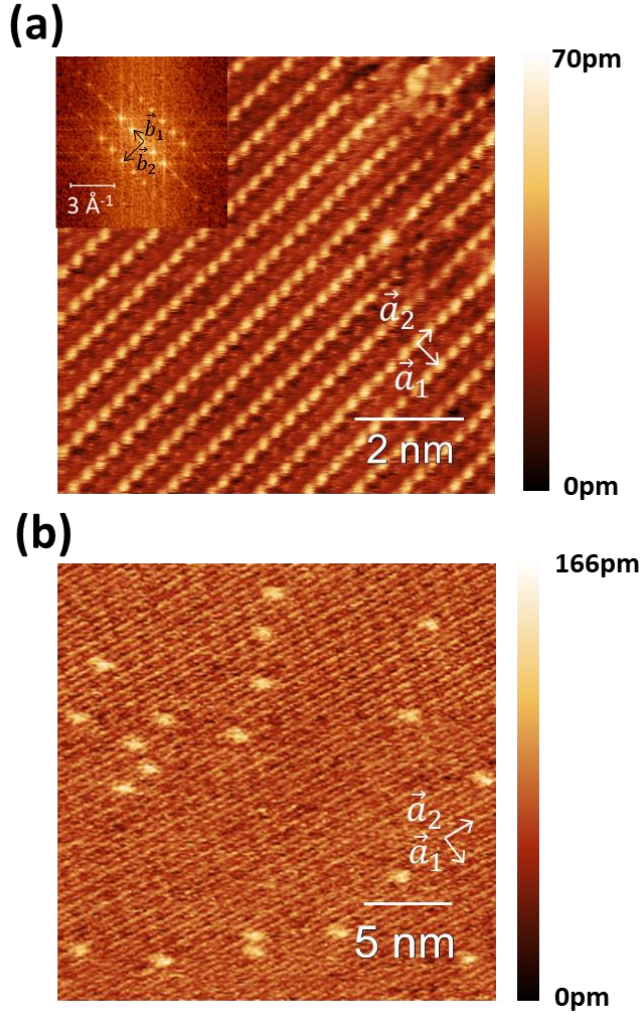


FIG. 6. STM topography of highly potassiated $K\text{-MoTe}_2$ (comparable to K_{255}) at room temperature. (a) Small-area scan with a bias voltage of +100 mV and a current setpoint of 70 pA. Figure inset: 2D FFT of the real space constant current image. (b) Larger-area scan with a bias voltage of +400 mV and a current setpoint of 10 pA. Unit cell vectors are not to the scale in (b).

To further test these findings, we turn to scanning tunneling microscopy. The constant current STM topography of the pristine substrate shows highly ordered rows of tellurium atoms, with a small number of atomic defects (See Fig. S7). After heavy potassiation, the same tellurium atom rows with occasional defects remain unchanged, as shown in Fig. 6 (a). 2D FFT of this and similar topography data reveal a periodic pattern with the reciprocal cell parameters of $\overline{FX} = 0.97 \text{ \AA}^{-1}$ and $\overline{FY} = 0.50 \text{ \AA}^{-1}$, corresponding to lattice vectors of $|\vec{a}_1| = 6.34 \text{ \AA}$ and $|\vec{a}_2| = 3.23 \text{ \AA}$, in excellent agreement with the

crystal structure of pristine 1T'-MoTe₂ [44]. This agrees also with DFT which shows that intercalation does not noticeably change these two dimensions. The STM image in Fig. 6 (b) captures the high degree of crystallinity over larger distances, but also manifests the appearance of larger bright protrusions (Fig. 6 (b)). The change of tip height along those bright protrusions amounts to an average of 41 ± 9 pm. Bright shallow protrusions of this kind have been assigned as a signature of potassium intercalation in the related WTe₂ [45]. We can, however, not exclude that some of these protrusions may rather be native defects also found in pristine MoTe₂ [46,47]. Crucially though, the STM topography does not carry signatures of potassium *surface adsorbates*, expected to lead to much larger height changes [45]. This is supported by previous STM studies of alkali atom depositions on 2D materials, where surface adsorbates are only observed at much lower sample temperatures, likely due to inhibition of intercalation at cryogenic temperatures [13,48-50]. Our data thus indicate that the population of surface-adsorbed potassium atoms is indeed very small or non-existent, fully consistent with our AD-XPS, ARPES and DFT results.

Discussion

In taking together all the experimental data and the DFT calculations, a consistent picture of the consequences of potassiation arises. Potassium atoms prefer intercalation over surface adsorption, swelling the c-axis of the crystal and eventually leading to layer decoupling, as can be seen from Fig 3 (b). As Fig. 1 and 2 demonstrate, this causes significant evolution of the band structure. An occupancy number of three or higher is thermodynamically stable, consistent with our ARPES results which prefer half-filling (occupancy number of four) over surface adsorption or full filling. Excess K atoms are driven deeper into the bulk crystal, intercalating between layers farther away from the surface (see e.g. Fig. 5 (b) and Fig S7) to maximize thermodynamic gain. As long as there is room for potassium atoms to diffuse in bulk, the lattice maintains a partial filling likely around an occupancy number of four. We

suggest that this intercalated phase is therefore a robust phase in the presence of finite amounts of K, and leads to layer-decoupling.

The UPS spectrum of K15 at \bar{Y} indicates that the Lifshitz transition occurs already at low potassium dosing, in what we termed the rigid band shift limit. This indicates that the Lifshitz transition is a separate process, apart from the band structure evolution and layer decoupling observed at higher dosing. This offers opportunities for the Fermiology of K-intercalated MoTe₂, as changes in the Fermi surface and the associated Lifshitz transition are typically accompanied by a sudden onset of new many-body processes that are not observed in the pristine host material. Indeed, a recent study of monolayer 1T'-MoTe₂ on graphene [51] demonstrates the emergence of charge order as a result of a partial charge transfer from graphene to MoTe₂, where the nesting vector aligns with the \bar{X} axis. In a similar fashion, the Lifshitz transition in bulk 1T'-MoTe₂ observed here may also lead to new correlated phenomena.

Alternative sources for the origin of the electron pocket at \bar{Y} , different from a Lifshitz transition, should be considered as well. Possible mechanisms include the formation of a free electron band [49], surface potential-induced band bending of the bulk band [13], or the formation of quantum well states as a result of multilayer potassium adsorbate formation [50]. These interpretations are however rather unlikely: First, the electron pocket appears at a high symmetry point away from $\bar{\Gamma}$. The formation of a free electron band or a quantum well away from the center of the Brillouin zone can only occur if other scattering processes are at play [52], and there is no evidence for such scattering. Second, we observe intercalation of potassium atoms rather than significant surface adsorption, rendering a multilayer potassium adsorbate rather unlikely. Though as demonstrated by our DFT results for the high potassium limit, we find no necessity to adjust the on-site Coulomb potential, the fact that the Lifshitz transition originates from potassium suggests an important role of electron correlation. Indeed,

ultrafast laser excitation has been reported to cause a reduction of the on-site Coulomb potential, resulting in a Lifshitz transition similar to the one observed here [10].

Our findings are also important to understand opportunities to access Weyl points at room temperature. Electron transfer from potassium upon intercalation may generate a vertical electric field in the 2D sheets which would break inversion symmetry without the need for inducing a structural shear displacement to the T_d phase. Based on the observed band shifts in our ARPES data, we speculate that it may be possible to shift the Weyl points which are above E_F in T_d MoTe₂ to below E_F using intercalation with a strong electron dopant. This may induce a topological phase transition to a new room temperature Weyl phase, at least in the first few potassiated layers. It is however known that perturbations to the pristine crystal lattice can change the number of Weyl points or even eliminate them [53-55] and potassium intercalation may do so. Also, our study suggests that large degrees of potassiation in fact suppress the presence of a hole pocket, which in turn would suppress the Weyl phase. Nevertheless, we believe that proximitization and intercalation with adsorbates has the potential to manipulate electronic and potentially topological phase transitions.

Conclusions

To conclude, our results show that the different stages of potassiation lead to distinctive changes in the electronic structure of the layered semimetal $1T'$ -MoTe₂. The measured ARPES spectra show the band structure progression from monotonic rigid band shifts to complex band structure evolution. A Lifshitz transition occurs already at low K dosing, independent of the band structure evolution at high potassium dosing. Our DFT study clearly shows that intercalation is preferred over surface adsorption, with an occupancy number near half-filling preferred. The lack of significant surface adsorption and the preference for intercalation is also confirmed by AD-XPS and STM. Using our combined theory and

multi-experiment approach, we thus demonstrate that the intercalation of potassium atoms can generate overall substantial band structure changes. Atomic intercalation may thus offer new avenues for tailoring electronic and topological phases.

References

- [1] J. Yang, J. Colen, J. Liu, M. C. Nguyen, G.-w. Chern, and D. Louca, *Science Advances* **3**, eaao4949 (2017).
- [2] C. Zhao, M. Hu, J. Qin, B. Xia, C. Liu, S. Wang, D. Guan, Y. Li, H. Zheng, and J. Liu, *Physical Review Letters* **125**, 046801 (2020).
- [3] J. Kim, S. S. Baik, S. H. Ryu, Y. Sohn, S. Park, B.-G. Park, J. Denlinger, Y. Yi, H. J. Choi, and K. S. Kim, *Science* **349**, 723 (2015).
- [4] Y. Wang, J. Xiao, H. Zhu, Y. Li, Y. Alsaïd, K. Y. Fong, Y. Zhou, S. Wang, W. Shi, and Y. Wang, *Nature* **550**, 487 (2017).
- [5] W.-M. Zhao, L. Zhu, Z. Nie, Q.-Y. Li, Q.-W. Wang, L.-G. Dou, J.-G. Hu, L. Xian, S. Meng, and S.-C. Li, *Nature Materials* **21**, 284 (2022).
- [6] W. Tao, Z. J. Tong, A. Das, D.-Q. Ho, Y. Sato, M. Haze, J. Jia, Y. Que, F. Bussolotti, K. E. J. Goh, B. Wang, H. Lin, A. Bansil, S. Mukherjee, Y. Hasegawa, and B. Weber, *Physical Review B* **105**, 094512 (2022).
- [7] N. Briggs, B. Bersch, Y. Wang, J. Jiang, R. J. Koch, N. Nayir, K. Wang, M. Kolmer, W. Ko, and A. De La Fuente Duran, *Nature Materials* **19**, 637 (2020).
- [8] J. Park, A. N. Batyrkhanov, J. Schaibley, and O. L. Monti, arXiv preprint arXiv:2308.05886 (2023).
- [9] B. Arnoldi, S. L. Zachritz, S. Hedwig, M. Aeschlimann, O. L. Monti, and B. Stadtmüller, arXiv preprint arXiv:2304.10237 (2023).
- [10] S. Beaulieu, S. Dong, N. Tancogne-Dejean, M. Dendzik, T. Pincelli, J. Maklar, R. P. Xian, M. A. Sentef, M. Wolf, A. Rubio, L. Rettig, and R. Ernstorfer, *Science Advances* **7**, eabd9275 (2021).
- [11] L. Stojchevska, I. Vaskivskiy, T. Mertelj, P. Kusar, D. Svetin, S. Brazovskii, and D. Mihailovic, *Science* **344**, 177 (2014).
- [12] Z. El Youbi, S. W. Jung, S. Mukherjee, M. Fanciulli, J. Schusser, O. Heckmann, C. Richter, J. Minár, K. Hricovini, and M. D. Watson, *Physical Review B* **101**, 235431 (2020).
- [13] O. J. Clark, F. Mazzola, J. Feng, V. Sunko, I. Marković, L. Bawden, T. K. Kim, P. King, and M. S. Bahramy, *Physical Review B* **99**, 045438 (2019).
- [14] C. Habenicht, J. Simon, M. Richter, R. Schuster, M. Knupfer, and B. Büchner, *Physical Review Materials* **4**, 064002 (2020).
- [15] C. N. Eads, S. L. Zachritz, J. Park, A. Chakraborty, D. L. Nordlund, and O. L. Monti, *The Journal of Physical Chemistry C* **124**, 19187 (2020).
- [16] M. Kang, B. Kim, S. H. Ryu, S. W. Jung, J. Kim, L. Moreschini, C. Jozwiak, E. Rotenberg, A. Bostwick, and K. S. Kim, *Nano Letters* **17**, 1610 (2017).
- [17] D. Qian, D. Hsieh, L. Wray, E. Morosan, N. Wang, Y. Xia, R. Cava, and M. Hasan, *Physical Review Letters* **98**, 117007 (2007).
- [18] E. Sajadi, T. Palomaki, Z. Fei, W. Zhao, P. Bement, C. Olsen, S. Luescher, X. Xu, J. A. Folk, and D. H. Cobden, *Science* **362**, 922 (2018).
- [19] S. Nishihaya, M. Uchida, Y. Nakazawa, M. Kriener, Y. Kozuka, Y. Taguchi, and M. Kawasaki, *Science Advances* **4**, eaar5668 (2018).
- [20] Y. M. Blanter, M. Kaganov, A. Pantsulaya, and A. Varlamov, *Physics Reports* **245**, 159 (1994).
- [21] A. Rossi, G. Resta, S. H. Lee, R. D. Redwing, C. Jozwiak, A. Bostwick, E. Rotenberg, S. Y. Savrasov, and I. M. Vishik, *Physical Review B* **102**, 121110 (2020).
- [22] R. Clarke, E. Marseglia, and H. Hughes, *Philosophical Magazine B* **38**, 121 (1978).
- [23] J. Jiang, Z. Liu, Y. Sun, H. Yang, C. Rajamathi, Y. Qi, L. Yang, C. Chen, H. Peng, and C. Hwang,

Nature Communications **8**, 13973 (2017).

- [24] F. Chen, H. Lv, X. Luo, W. Lu, Q. Pei, G. Lin, Y. Han, X. Zhu, W. Song, and Y. Sun, *Physical Review B* **94**, 235154 (2016).
- [25] Q. Zhou, D. Rhodes, Q. Zhang, S. Tang, R. Schönemann, and L. Balicas, *Physical Review B* **94**, 121101 (2016).
- [26] Y. M. Itahashi, Y. Nohara, T. Ideue, T. Akiba, H. Takahashi, S. Ishiwata, and Y. Iwasa, *Physical Review Research* **5**, L022022 (2023).
- [27] T. Wang, X. Luo, J. Gao, Z. Jiang, W. Wang, X. Yang, N. Zhou, X. Zhu, L. Zhang, and W. Lu, *Advanced Materials* **35**, 2208800 (2023).
- [28] F. Sojka, M. Meissner, C. Zwick, R. Forker, and T. Fritz, *Review of Scientific Instruments* **84** (2013).
- [29] G. Kresse and J. Furthmüller, *Computational Materials Science* **6**, 15 (1996).
- [30] G. Kresse and J. Hafner, *Physical Review B* **48**, 13115 (1993).
- [31] P. E. Blöchl, *Physical Review B* **50**, 17953 (1994).
- [32] G. Kresse and D. Joubert, *Physical Review b* **59**, 1758 (1999).
- [33] J. P. Perdew, K. Burke, and M. Ernzerhof, *Physical Review Letters* **77**, 3865 (1996).
- [34] A. Tkatchenko, R. A. DiStasio Jr, R. Car, and M. Scheffler, *Physical Review Letters* **108**, 236402 (2012).
- [35] T. Huempfer, F. Otto, T. Fritz, and R. Forker, *Advanced Materials Interfaces* **9**, 2200585 (2022).
- [36] N. Aryal and E. Manousakis, *Physical Review B* **99**, 035123 (2019).
- [37] J.-H. Lee and Y.-W. Son, *Physical Chemistry Chemical Physics* **23**, 17279 (2021).
- [38] J. Hwang, C. Zhang, and K. Cho, *2D Materials* **4**, 045012 (2017).
- [39] X. Cui, H. Yan, X. Yan, K. Zhou, and Y. Cai, arXiv preprint arXiv:2305.12762 (2023).
- [40] C. Spataru, M. Witman, and R. Jones, *Physical Review Materials* **5**, 084005 (2021).
- [41] J. Chastain and R. C. King Jr, *Perkin-Elmer Corporation* **40**, 221 (1992).
- [42] A. Jablonski and C. Powell, National Institute of Standards and Technology, Gaithersburg (2010).
- [43] C. J. Powell, *Journal of Vacuum Science & Technology A* **38** (2020).
- [44] A. Tamai, Q. Wu, I. Cucchi, F. Y. Bruno, S. Riccò, T. K. Kim, M. Hoesch, C. Barreteau, E. Giannini, and C. Besnard, *Physical Review X* **6**, 031021 (2016).
- [45] L. Zhu, Q.-Y. Li, Y.-Y. Lv, S. Li, X.-Y. Zhu, Z.-Y. Jia, Y. Chen, J. Wen, and S.-C. Li, *Nano Letters* **18**, 6585 (2018).
- [46] S.-H. Kang, S. Jeon, H.-J. Kim, W. Ko, S. Cho, S. H. Kang, S. W. Kim, H. Yang, H. W. Kim, and Y.-W. Son, *Physical Review B* **105**, 045143 (2022).
- [47] P. Rüßmann, A. Weber, F. Glott, N. Xu, M. Fanciulli, S. Muff, A. Magrez, P. Bugnon, H. Berger, and M. Bode, *Physical Review B* **97**, 075106 (2018).
- [48] T. Han, L. Chen, C. Cai, Z. Wang, Y. Wang, Z. Xin, and Y. Zhang, *Physical Review Letters* **126**, 106602 (2021).
- [49] T. Eknapakul, I. Fongkaew, S. Siriroj, R. Vidyasagar, J. Denlinger, L. Bawden, S.-K. Mo, P. King, H. Takagi, and S. Limpijumngong, *Physical Review B* **94**, 201121 (2016).
- [50] N. Alidoust, G. Bian, S.-Y. Xu, R. Sankar, M. Neupane, C. Liu, I. Belopolski, D.-X. Qu, J. D. Denlinger, and F.-C. Chou, *Nature Communications* **5**, 4673 (2014).
- [51] L.-X. Wei, P.-C. Xiao, F. Li, L. Wang, B.-Y. Deng, F.-J. Cheng, F.-W. Zheng, N. Hao, P. Zhang, and X.-C. Ma, arXiv preprint arXiv:2308.11101 (2023).
- [52] S.-J. Tang, Y.-R. Lee, S.-L. Chang, T. Miller, and T.-C. Chiang, *Physical Review Letters* **96**, 216803 (2006).

- [53] Z. Wang, D. Gresch, A. A. Soluyanov, W. Xie, S. Kushwaha, X. Dai, M. Troyer, R. J. Cava, and B. A. Bernevig, *Physical Review Letters* **117**, 056805 (2016).
- [54] I. Belopolski, T. A. Cochran, X. Liu, Z.-J. Cheng, X. P. Yang, Z. Guguchia, S. S. Tsirkin, J.-X. Yin, P. Vir, and G. S. Thakur, *Physical Review Letters* **127**, 256403 (2021).
- [55] T.-R. Chang, S.-Y. Xu, G. Chang, C.-C. Lee, S.-M. Huang, B. Wang, G. Bian, H. Zheng, D. S. Sanchez, I. Belopolski, N. Alidoust, M. Neupane, A. Bansil, H.-T. Jeng, H. Lin, and M. Zahid Hasan, *Nature Communications* **7**, 10639 (2016).

Supplemental Materials

Lifshitz Transition and Band Structure Evolution in Alkali Metal Intercalated 1T'-MoTe₂

Joohyung Park,¹ Ayan N. Batyrkhanov,¹ Jonas Brandhoff,³ Marco Gruenewald,³ Felix Otto,³ Maximilian Schaal,³ Saban Hus,⁴ Torsten Fritz,^{1,3} Florian Göttl,² An-Ping Li⁴, and Oliver L.A. Monti^{1,5,*}

Affiliations

¹ Department of Chemistry and Biochemistry, University of Arizona, Tucson, Arizona, 85721, USA

² Department of Biosystems Engineering, University of Arizona, Tucson, Arizona, 85721, USA

³ Institute of Solid State Physics, Friedrich Schiller University Jena, 07743 Jena, Germany

⁴ Center for Nanophase Materials Sciences, Oak Ridge National Laboratory, Oak Ridge, Tennessee 37831, USA

⁵ Department of Physics, University of Arizona, Tucson, Arizona, 85721, USA

Fig. S1 LEED Pattern of Pristine 1T'-MoTe₂

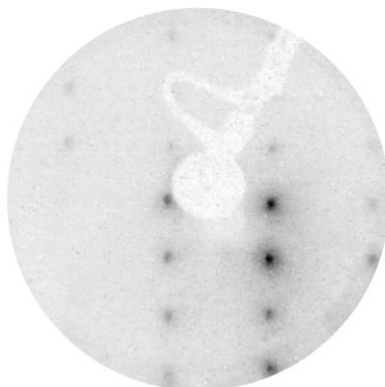


FIG. S1. Distortion-corrected LEED pattern of pristine 1T'-MoTe₂ with electron energy of 80 eV. Residual stray magnetic fields dim diffraction spots in the lower left corner.

Fig. S2 Shape of Electron Pocket with Two Different Color Contrasts

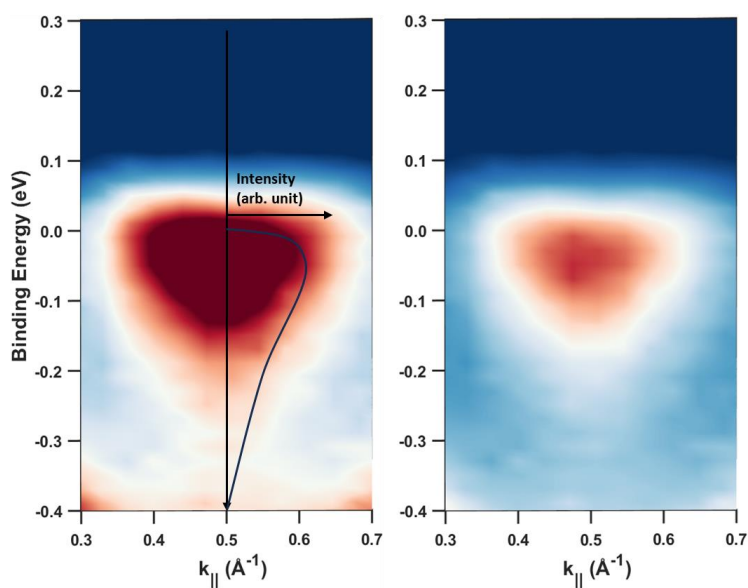


FIG. S2. ARPES map of the electron pocket at \bar{Y} for K210. Both figures show the same pocket, shown with different color contrast. Left: Saturated color contrast to highlight the tail at higher binding energy. The black line represents a guide to the eye for the energy-dependent intensity distribution. Right: Regular color contrast.

Fig. S3 DFT Parametrization of Layer Separation and Hubbard U and Fig. S4 Comparison Between ARPES and Slab Calculation Band Structure of Pristine 1T'-MoTe₂

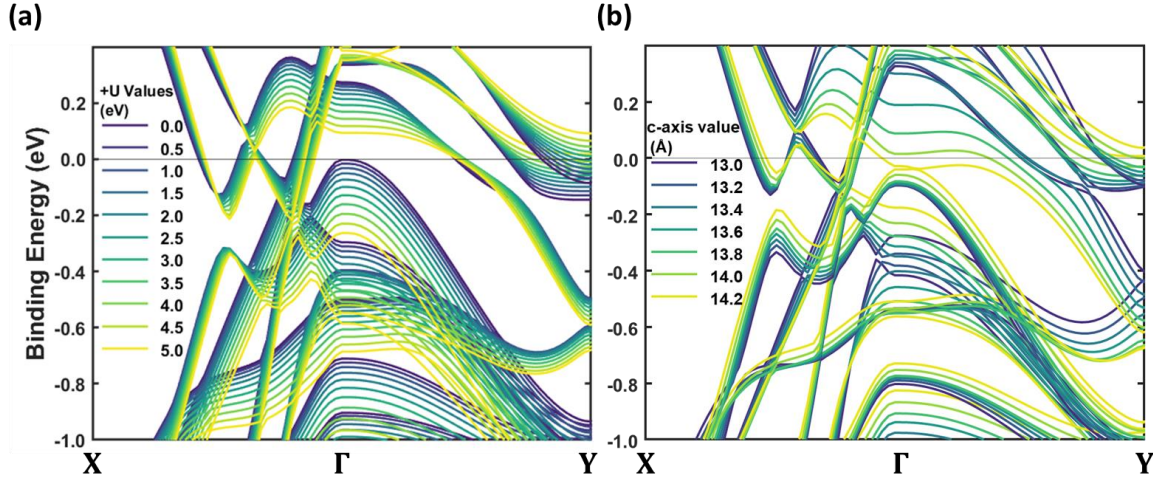


FIG. S3. Parametrization of the DFT band structure of pristine 1T'-MoTe₂ along the two high symmetry directions $\overline{\Gamma X}$ and $\overline{\Gamma Y}$ by changing (a) +U, with a unit cell c-axis value of 13.4 Å, and (b) the unit cell c-axis value with a fixed value +U of 1.5 eV. The colors correspond to different parameter values. See text below for the detailed procedure.

One of the major challenges in performing band structure calculations for MoTe₂ is to correctly describe the energies of the Mo d-states, since the PBE-functional is known to underestimate the gap between these states. One way to address this shortcoming is to artificially increase the separation between the d-states using the +U method. Several different U values for the Mo d-states have been suggested, but no agreement on the correct U value has been reached for MoTe₂ [1-3]. In addition, the calculated band structures also depend on the layer separation in MoTe₂. We use a dispersion correction as parameterized by Tkatchenko and Scheffler [4], which overestimates dispersion corrections for the MoTe₂ system and significantly underestimates the layer separation compared to the experimentally known crystal structure.

To address these shortcomings, we parameterize (i) the +U parameter and (ii) the layer separation in MoTe₂ for the 1T' phase of MoTe₂. These two parameters and their effects are independent

of each other. For this phase in particular, the experimentally observed absence of an electron pocket around the Fermi level at \bar{Y} is an important feature that is not correctly reproduced by pure PBE [3], and we use this as an indicator for the parametrization.

First, we vary the +U parameter for the Mo 3d states between 0.0 eV and 5.0 eV. The results are shown in Figure S3(a). We find that all bands are significantly impacted by the +U. Most bands are increasingly shifted to lower energies with +U, only the unoccupied bands around \bar{Y} are shifted to rise above the Fermi level. At the highest +U value, the bands at the \bar{Y} point start to lie above the Fermi level, as required by the experimental data.

We then fix the +U value at +1.5 eV and varied the z -distance of the unit cell between 13.0 Å and 14.2 Å (see Figure S3(b)). Here, some bands shift to higher energies, while other bands shift to lower energies, and some bands remain almost unchanged. Focusing again on the bands close to the Fermi level at \bar{Y} , we find that these bands are shifted to higher energies with increased layer separation, but only at 14.2 Å do all bands lie above the Fermi level. We then iterate this procedure, adjusting +U and the c -axis value, with a slab calculation method (see Fig. 4 and related main text for details, see other results using slab calculations in Fig. S5) until an optimal match with the experimental ARPES band structure is achieved. Overall, we find that +U of 2.0 eV and layer separation of 14.2 Å offer the best agreement with the ARPES map of pristine 1T'-MoTe₂ shown in Figure S4.

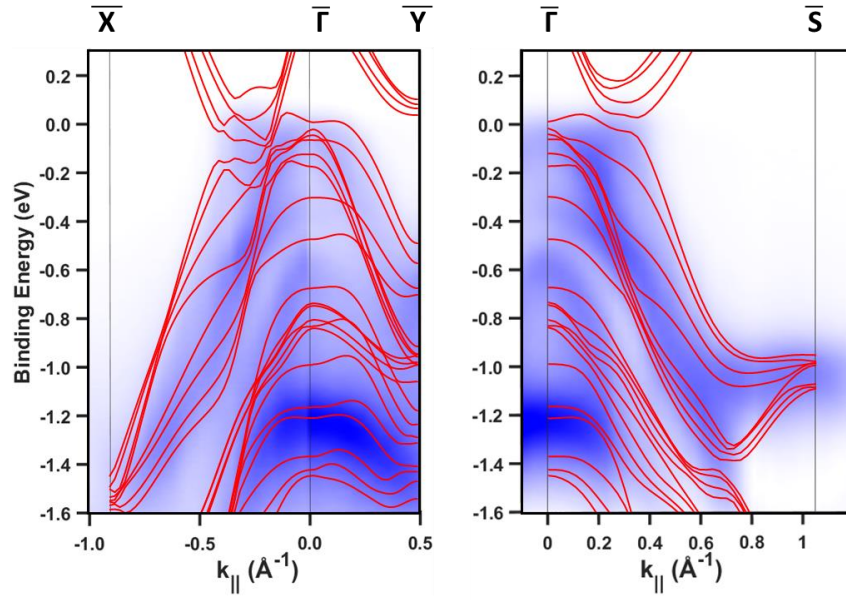


FIG. S4. Comparison between the optimized slab calculation band structure and the experimental band structure of pristine 1T'-MoTe₂. Left: $\bar{\Gamma}\bar{X}$ and $\bar{\Gamma}\bar{Y}$. Right: $\bar{\Gamma}\bar{S}$.

Fig S5 DFT Optimized Crystal and Band Structures Using Slab Calculation for Intercalation and Surface Adsorbate Scenarios

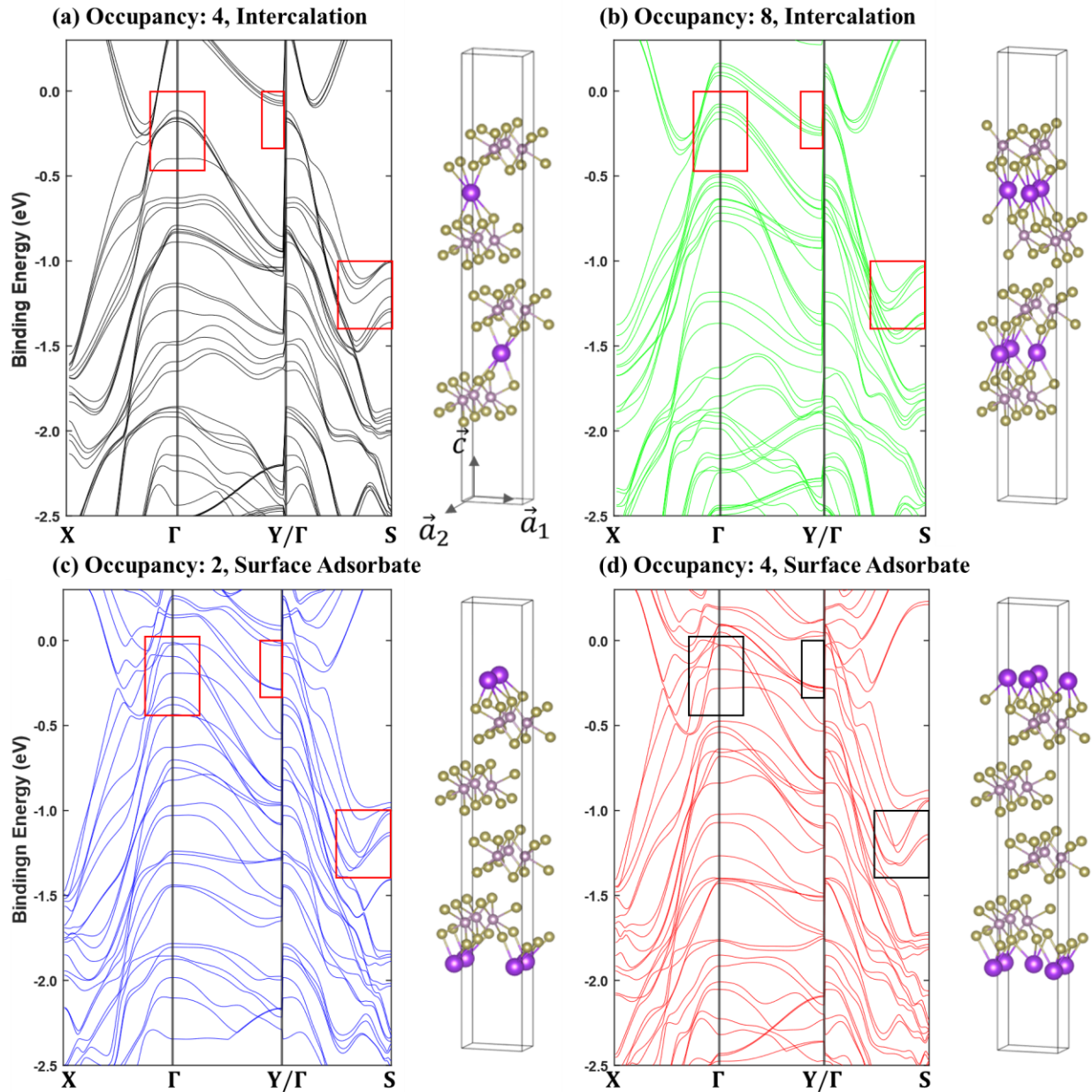


FIG. S5. DFT slab calculations of crystal and band structures for select potassium occupation numbers. (a) The preferred intercalation scenario with an occupancy number of four. Other cases: (b) Intercalation scenario with an occupancy number of eight., i.e. the maximum potassium occupation number. (c) Surface adsorbate scenario with an occupancy number of two. (d) Surface adsorbate scenario with an occupancy number of four (maximum number for surface adsorbate). Red boxes (black boxes in S5 (d)) indicate the region where marked differences appear.

We use a slab calculation method to investigate the band structure of $1\Gamma'$ -MoTe₂ with different

potassium occupancy numbers and occupation configurations, namely intercalation and surface adsorbate to assess the most likely experimental scenario. The presented results in Fig. S5 are optimized with the procedure mentioned in the main text. Here we show a selection of scenarios that can be ruled out and the preferred case of occupancy number of four (half-filling, 0.5 K / Mo). An intercalation occupancy number of 8 (full filling, 1.0 K / Mo) supports an excessively pronounced electron pocket at Y (Figure S5 (b)), as well as the absence of a flat band near -0.4 eV at Γ . The surface adsorbate scenarios can also be readily rejected: The absence of an electron pocket at \bar{Y} for the full occupancy (full filling, 1.0 K / Mo) in Figure S5 (d) does not match with the ARPES data, and many bands at Γ do not fit well with the experimental ARPES data. In the case of half-filling of the surface sites (occupancy number of 2, 0.5 K / Mo) in Figure S5 (c), many bands at the high symmetry points Γ , Y , and S are missing in the experimental data.

Fig S6 Impact of Higher Potassiation

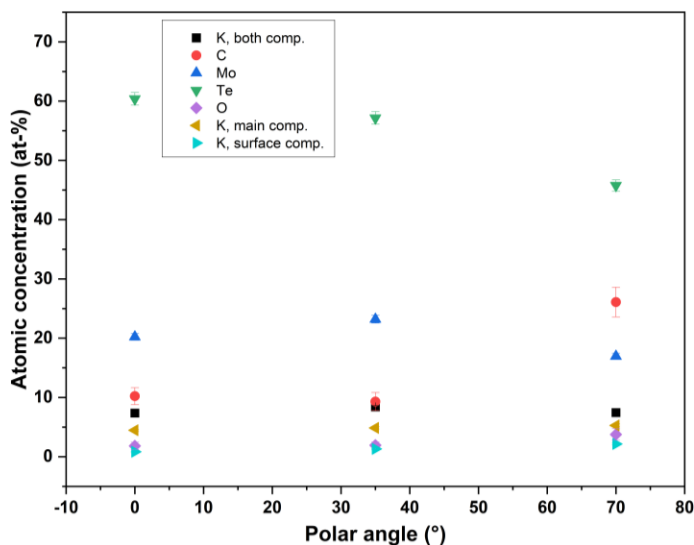


FIG. S6. AD-XPS of overdosed K-MoTe₂, showing the atomic concentration of detected elements over select polar (photoemission) angles for a sample with double the potassium load of Figure 5 (b) in the main text.

Over the angles we investigated, the K/Mo ratio determined from the values in Figure S6 is nearly identical to those shown in Figure 5 (b) in the main text. It should be noted that the amount of potassium deposited in the sample is twice that in Figure 5 (b). This suggests that thermodynamic equilibrium forces extra potassium atoms to diffuse into deeper layers.

S.7 STM Topography Image of Pristine 1T'-MoTe₂ at Room Temperature

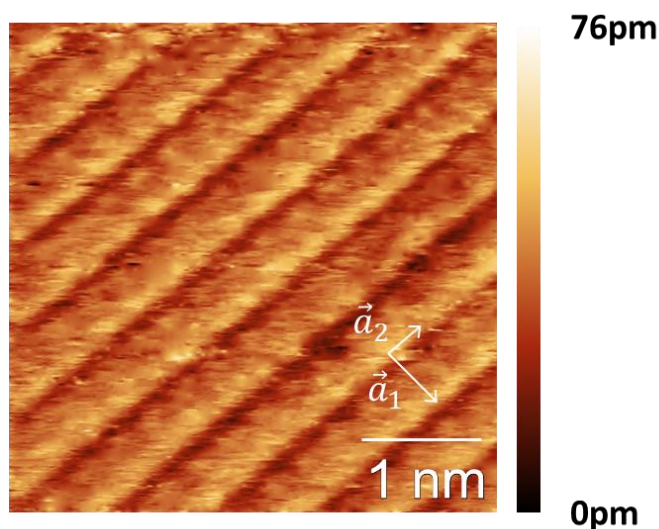


FIG. S7. STM image of pristine 1T'-MoTe₂ at room temperature with a bias voltage of +150 mV and a current setpoint of 1 nA. Unit cell vector labels are identical to the ones in the main text.

References

- [1] N. Aryal and E. Manousakis, *Physical Review B* **99**, 035123 (2019).
- [2] S. Beaulieu, S. Dong, N. Tancogne-Dejean, M. Dendzik, T. Pincelli, J. Maklar, R. P. Xian, M. A. Sentef, M. Wolf, and A. Rubio, *Science Advances* **7**, eabd9275 (2021).
- [3] N. Xu, Z. Wang, A. Magrez, P. Bugnon, H. Berger, C. E. Matt, V. N. Strocov, N. C. Plumb, M. Radovic, and E. Pomjakushina, *Physical Review Letters* **121**, 136401 (2018).
- [4] A. Tkatchenko, R. A. DiStasio Jr, R. Car, and M. Scheffler, *Physical Review Letters* **108**, 236402 (2012).